FABRICATION OF SOLAR ABSORBER TUBE WITH INTERNAL FIN STRUCTURE WITH IN718 AND EFFECT OF BORON WITH IN718 FOR SOLAR ABSORBER TUBE USING SELECTIVE LASER MELTING 3D PRINTING TECHNOLOGY

A Thesis

by

NAZNIN NURIA AFRIN

Submitted in Partial Fulfillment of the

Requirements for the Degree of

MASTER OF SCIENCE IN ENGINEERING

Major Subject: Manufacturing Engineering

The University of Texas Rio Grande Valley

December 2022

FABRICATION OF SOLAR ABSORBER TUBE WITH INTERNAL FIN STRUCTURE WITH IN718 AND EFFECT OF BORON WITH IN718 FOR SOLAR ABSORBER TUBE USING SELECTIVE LASER MELTING 3D PRINTING TECHNOLOGY

A Thesis
by
NAZNIN NURIA AFRIN

COMMITTEE MEMBERS

Dr. Jianzhi Li
Chair of Committee

Dr. Farid Ahmed
Committee Member

Dr. Zhaohui Geng
Committee Member

December 2022

ABSTRACT

Afrin, Naznin Nuria, Fabrication of Solar Absorber Tube with Internal Fin Structure with IN718 and effect of Boron with IN718 for Solar Absorber Tube using Selective Laser Melting 3D printing Technology. Master of Science in Engineering (MSE), December, 2022, 74 pp., 11 tables, 38 figures, references, 93 titles.

This research aimed to fabricate Solar Absorber Tubes for Solar-Thermal Power Plant with internal fin structures using Selective Laser Melting (SLM) technology. In this study, we investigated the effect of B with IN718 in 3D printing using SLM for solar absorber tubes. The objective was to study the material-process-properties relationship with goal to identify and validate the optimal parameters for the SLM process. Material selected for this study was IN718 with 0.5% and 1% B particle mixed using a V-shape mixing machine. The flowability test was conducted using the Angle of Repose (AOR) method. 3D printed samples were fabricated with mixed powder under different energy densities using different parameter settings. The microstructure of these 3D printed samples was observed using an Optical Microscope. The goal of this study included mixing different percentages of B with In718, fabrication of 3D printed sample and optimizing its process parameters to observe the surface morphology, optical properties, and microstructure to investigate the effect of B with IN718 for the solar absorber tube.

DEDICATION

I want to dedicate all my achievements to my family for believing in me. I promise to make you proud. Whenever I had pressure of multiple tasks at the same deadline, whenever I felt tired, they gave me mental strength. The journey was not easy, but all your support and confidence made me confident too. Thank you for your love and patience.

ACKNOWLEDGMENTS

This research work was supported by the US Department of Energy under SETO 2020-SIPS program. I am extremely grateful to Dr. Jianzhi (James) Li, chair of my thesis committee, advisor, and professor, for guiding and mentoring me. I will forever be grateful to Dr. Jianzhi (James) Li, for believing in me and providing the resources needed for me to succeed. I also want to thank Dr. Shanshan Zhang, Dr. Farid Ahmed, Dr. Zhaohui Geng, Dr. Ben Xu, and Dr. Jacob Lee for giving me all the guidance and helping me in the lab whenever I needed help. Thanks to all my lab mates and friends who made my time at the lab a great experience. A special thank you to Dr. Victoria Padilla who was kind enough to help with EDS and SEM analysis and Mr. Oscar Martinez for helping with administrational information for the necessary lab equipment.

TABLE OF CONTENTS

Page

LIST OF TABLES

Page

LIST OF FIGURES

Page

CHAPTER I

INTRODUCION

Background and Overview

In the Concentrating Solar Power (CSP) system, solar energy is absorbed in the receivers which are concentrated panels of absorber of cylindrical shape, usually placed on the top of the solar tower [18, 21]. The main components are i) thermal power storage ii) the solar concentrating system and iii) the absorber tube [22]. Figure 1 shows a Concentrated Solar Power plant where thermal energy from sunlight is captured by thousands of mirrors which is called heliostat. In the center of this heliostat, a tower is implemented, and the solar absorber tube resides on top of this solar tower. When the molten salt get heated by the sunlight, it flows towards the thermal power storage tank and eventually starts pumping to the steam generator. The steam from the steam generator starts driving the turbine and generates electricity [90].

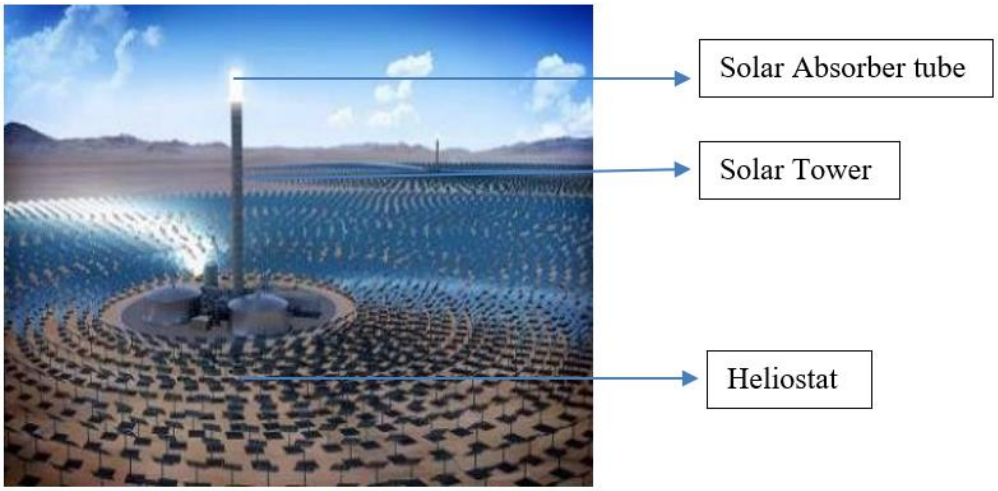

Figure 1: Concentrated Solar Power Plant [90]

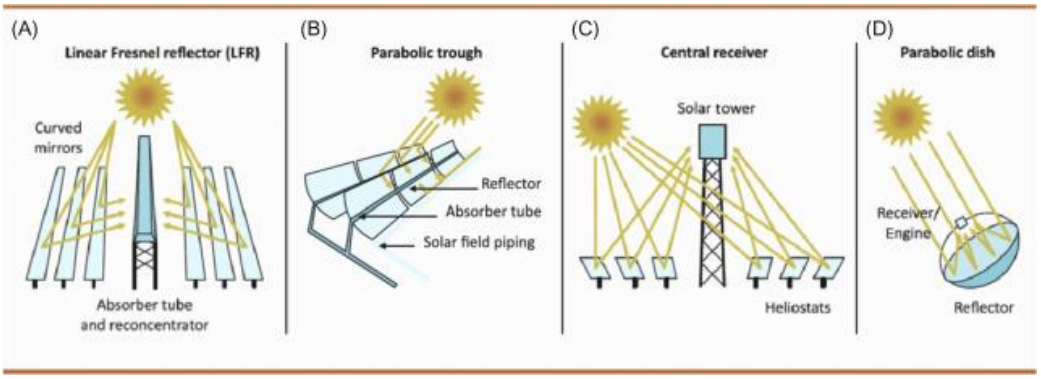

Figure 2: Types of commercial Concentrated Solar Power Plant [88]

Figure 2 shows the most popular four types of commercial CSP system. Linear Fresnel Reflector (LFR), and Parabolic trough as shown in figure 2(a) and (b), are for concentrating the light on the linear receiver. These first two commercial receivers are usually made of steel tubes and the temperature range is around 400 °C, and thermal oil use as the working fluid [88]. Central receiver and parabolic dish as shown in figure 2 (c), and (d), are for concentrating the solar light to the point receiver. The central receiver has a temperature range between 600 °C- 1200°C, while the parabolic dish has a temperature range of 800°C [88].

Current state of art for the CSP and the Manufacturing processes

The heat transfer efficiency and performance of the solar collector depends on which material is used in the solar absorber and how efficient the design is [89]. Materials for solar absorber tubes are being selected based on their capacity to withstand a wide range of distribution of temperature, efficient properties to transfer heat to obtain the heat flux at its maximum value. The geometry and design of the absorber tube has a vital role in solar heat transfer efficiency [88]. Oxide ceramics are considered as good materials for high temperature such as 800 °C, but they have poor optical properties [89]. Optical properties of the CSP system refer to the amount of solar

light absorbed to its receiver tower, or how much it's reflecting and transmitting [93]. Material selection for CSP has been an increasing and broad

area of research as the material with higher sunlight absorptivity will enhance the optical performance for the solar absorber tube [93]. Better optical performance provides higher solar absorptivity, and less emissivity hence improves the overall performance of CSP system [92]. To improve this optical performance for solar absorber tubes, coating the tube with higher solar absorptive material has considered in some CSP systems, but practical implementation of this idea is very expensive and not a permanent solution as the coating fades away with hours of operations [93]. Instead of coating the low thermally stable material, researchers are more interested in finding out a suitable material which can provide higher optical performance. There are some other existing materials that are in use for the absorber tubes that are also having issues with either thermal properties or porosity or low mechanical properties [92]. Because of these issues, ongoing research on optimal materials for solar absorber tubes is being more focused on overcoming these problems related to material performance.

Figure 3 shows a Molten-salt central receiver system with cylindrical tubular receiver. The irradiation of a solar receiver can be direct or indirect and it depends on what kind of solar absorbing material is in use for the energy transfer process through the molten salt [92]. The stream of working fluids used in the direct irradiation receiver can absorb the concentrated heat flux efficiently by the stream flow [92]. While in the indirect receiver such as tubular absorber works in heat exchange mechanism where inside the absorber tube, the cooling thermal molten salt flows and collects heat to the steam generator as shown in figure 3. This heat exchange rate depends on the absorbing material selection and appropriate working condition [92]. Absorbing materials at the high temperature operating conditions, loss the heat flux by emission at the solar receiver, depending on their thermal stability and it leads to low production of electricity [92].

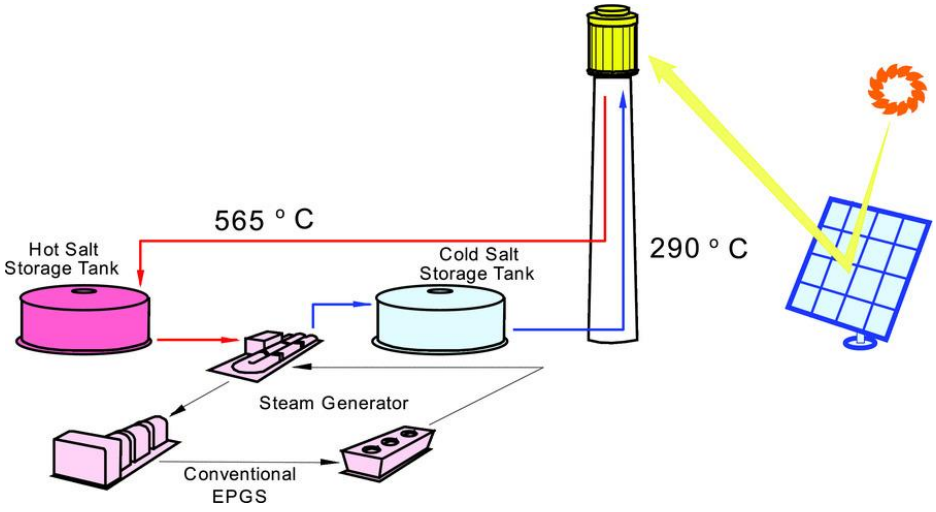

Figure 3: Molten-salt central receiver system with cylindrical tubular receiver [92]

The materials used in the existing absorber tubes are accountable for the damage due to corrosion or creep fatigue, enhanced by high temperature [92]. This chapter introduces an overview of the required microstructural properties of the materials for solar absorber tubes, defines the problem statement, describes research questions and objectives. It is important to research the material properties of the solar absorber tube for better performance. Good microstructure and optical properties for application in high temperatures and high operating pressure are very important. Also, the material has to be a good corrosion-resistant material. A high thermally conductive material such as Aluminum, Copper shows poor mechanical properties in high temperature and pressure of a solar plant operating condition. Low alloyed stainless steels have better thermal energy conductivity than highly alloyed stainless steel, but these steels are low corrosion-resistant [18].

The temperature distribution depends on the material properties of the tube [37]. This study aims to fabricate Solar Absorber Tubes with internal fin structures to provide uniform temperature distribution. In this Thesis, we aimed to study the effect of Boron with IN718 to improve the thermal and optical efficiency of the Solar Absorber Tube.

Problem Statement

Here are technical difficulties for high temperature solar absorber tube design and conventional manufacturing approach as mentioned in the current state of art of the CSP system. It is important to adopt an approach that will include necessary qualification criteria to promote more uniform temperature distribution. This Thesis research is funded by the US Department of Energy and the demand of this research project is to try adding internal fin structure to prevent heat damage due to non-uniform circumferential temperature distribution in the absorber tube. It improves the heat transfer performance drastically and prevents pressure loss. But in the current manufacturing process it is hard to have a permanent internal fin structure.

One of the main problems or challenges of a solar absorber tube in a solar power system is the induced stress due to high temperature gradient and pressure. Component fails due to high temperature during operations because the materials used in the solar absorber tubes are unable to withstand this very high temperature [4]. Eventually this thermal stress leads to structural deformation, fatigue, and creep. IN718 is resistant to high temperatures and stress such as tensile and creep properties. The temperature range for this alloy can reach around 750 °C [5]. Moreover, IN718 has high corrosion resistance. But constantly being exposed at the high temperature in the solar absorber tube causes thermal decomposition thus causes deterioration of microhardness and corrosion resistance [82].

Opportunities and Hypothesis

The challenges with current design and manufacturing method of solar absorber tubes for CSP system as mentioned above can be addressed with the Additive Manufacturing approach. With the development and capability of Additive Manufacturing to fabricate complex structures, there is a chance to fabricate the tube with internal fin structure all together. Opportunities enabled by metal Additive Manufacturing technology can be the solution to the existing problem of the CSP system. The laser process parameters of the SLM technology have a very vital role in microstructure of fabricated parts. Optimization of the process parameters for the solar absorber tube can improve the microstructural properties of the tube.

The materials used in the existing absorber tubes are accountable for the damage due to corrosion or creep fatigue, enhanced by high temperature. IN718 has great corrosion resistance and thermal stability, but as reported by the other researchers, this superalloy loses its thermal and microhardness properties over time due to operating at high temperature [79,80]. Adding a small amount of Boron with IN718 can enhance thermal and optical properties of the solar absorber tube as it has excellent thermo-mechanical properties [81,82]. We are also assuming that because of the darker shade of this material, it increases the solar absorptivity and decreases the solar emissivity.

Research Questions

To achieve this aim of the research, it is very important to know why this research is important and what is the significance of this research. The following questions are important for the continuity of the flow of this research, including:

1) What is the impact of adding B with IN718 to enhance the optical and microstructural performance of the solar absorber tube?
2) What will be the optimal laser parameter sets for the AM fabrication process to enhance the microstructural properties of the solar absorber tube?

CHAPTER II

LITERATURE REVIEW

Overview of Concentrating Solar Power system

Undoubtedly, the demand for clean energy is increasing drastically everyday as it improves health with less carbon emission. Thermal energy storage (THS) has the ability to meet this demand by heat storing and it is becoming a source for solar energy utilization, hence allowing Concentrated Solar Power to be highly reachable [19]. So, the demand for this method is the highest as it has the capacity to generate electricity in bulk, and power plant companies, researchers, and policymaking authorities are more interested in this technology [20]. The main components are i) thermal power storage ii) the solar concentrating system and iii) the absorber tube [22]. And this configuration cannot be achieved in the conventional method. Manufacturing sustainability can be achieved by minimizing material waste, and it can be obtained in additive manufacturing approach [23, 24]. The conventional method for solar-thermal power systems has some major issues which can't be overlooked, such as heat damage in the absorber tube which leads to an increase in the total manufacturing and maintenance cost [25]. To prevent the heat loss of a solar power system, additive manufacturing of the tubes with internal fin structure is one of the considerable approaches [27]. It improves the heat transfer performance drastically and prevents pressure loss [28]. The ultimate goal is to double the lifespan of the absorber tube and decrease the manufacturing, operation and maintenance cost by 50% compared to the conventional method [29]. Here are technical difficulties for high temperature solar absorber tube, neither installing, nor manufacturing the fin structure through conventional manufacturing approach can resolve the issue of non-uniform circumferential temperature

distribution [26]. So, it is important to adopt an approach that will include necessary qualification criteria to promote more uniform temperature distribution, such as Additive Manufacturing which can be applied to 3D print the entire solar absorber tube with internal structure.

Material selection for Solar Absorber Tube

The temperature distribution depends on the material properties of the tube [37]. The harsh operating conditions and high capital investment of the solar absorber tubes require an analysis of the life of an outdoor tubular molten salt receiver with five alternative tube alloys: Haynes 230, Alloy 316H, Inconel 625, 740H and 800H [37,38]. These selections are motivated from the outstanding corrosion and mechanical properties of the alloys [40,41,42]. Thermal analysis of these above-mentioned alloys was conducted by Laporte-Azcué, Marta, et al, by calculating the heat flux on the absorber tubes [37]. To achieve a precise solution, divisions of circumference of the tubes should be considered [43]. After carrying out the temperature distribution on tubes, strain and stress on the tubes were calculated with an analytical method by Laporte-Azcué et al [44]. Equivalent Operating Days (EOD) is a method to calculate the lifetime of solar absorber tubes which considers the creep and fatigue behavior and damage caused by them in a solar absorber tube, and Linear Damage Simulation (LDS) is widely use in this EOD procedure [45]. The literature study shows the LDS method conducted by Laporte-Azcué, Marta, et al as shown in figure 4 [37].

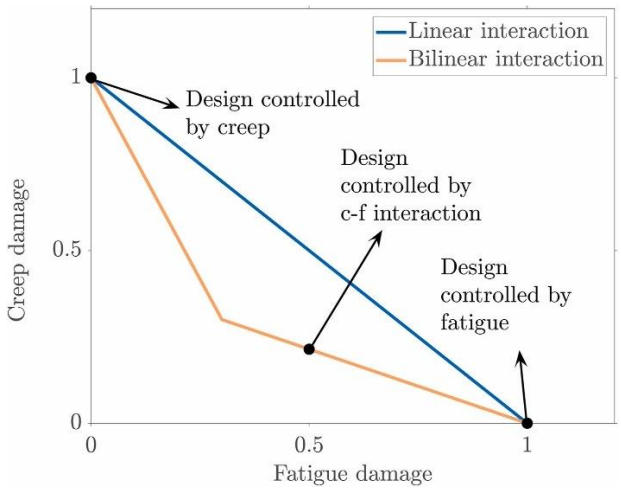

Figure 4: Fatigue-Creep Interaction [37]

Alloy 316H also known as SS316 a stainless-steel alloy has high temperature grade application, but less stress-corrosion efficiency [47].

IN625 has better corrosion resistance but working under 600 °C, also recommended annealing of the Absorber tubes [48]. Also, this alloy IN625 observes to have grain boundary precipitations even after low 12range [53].

Inconel 718 (IN718), a Nickel-based superalloy improves thermal and structural performances for Solar Power Plant due to its higher coefficient of thermal expansion [54]. Concentrated Solar Power (CSP) systems provide an elevated working temperature which is above 700 °C [55,56]. The main challenge of a Solar Absorber tube in a Solar Power System is the induced stress due to high temperature and pressure. According to research of Conroy et al. [57], the properties of the materials, specifically mechanical and thermal, used in Solar absorber Tubes for the Solar tower systems. IN718 offers outstanding thermal and mechanical properties which can withstand the elevated working temperature 700 °C for the Concentrated Solar Power system [54, 58]. Pure Nickel has higher conductivity, but very low mechanical properties compared to the Nickel superalloy 718. The relation between the alloys and conductivity of temperature are shown below. The summary from Table 1 shows that Inconel 718 has the better thermal conductivity.

Table 1

Thermal conductivity of superalloys.[54]

Superalloys	Thermal conductivity (W/(m·K))
Inconel 718 [59]	0.0156 T + 6.29
Nickel [60]	0.0212 T + 50.58
316 stainless steels [61]	0.0157 T + 9.28

Inconel 718

IN718 a Nickel-based superalloy is relatively new alloy, which is becoming more popular in Solar Power plants, aerospace and turbine application due to its highly corrosive resistance and thermal efficiency [4, 5]. The demand in the industry of IN718 is rapidly increasing as it has the ability to withstand harsh environmental conditions as it has highly efficient thermal, mechanical, and chemical properties [62].

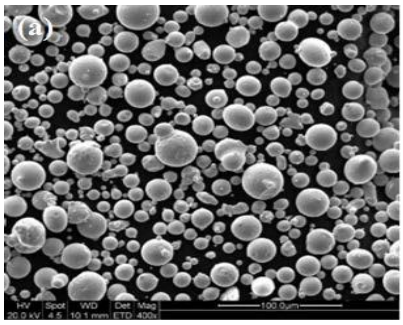

Figure 5: SEM Image of Inconel 718 [62]

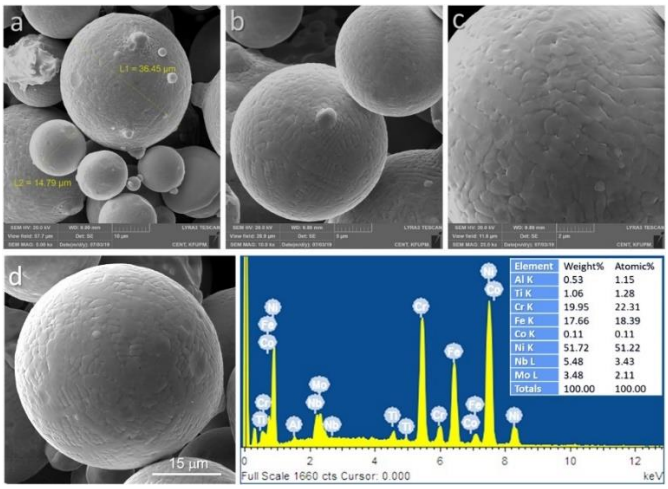

Figure 6: Morphology of powder (a), (b), (c), FESEM image of the particle (d), and EDX analysis (e) [62].

Composition of Inconel 718 is shown in Table 2[25].

Table 2

Composition of IN718

Elements	**GA**	**GA**	**PREP**	
Ni	BAL	53.05	54.82	51.75
Cr	18.4	18.23	18.08	19.68
Fe	17.7	17.58	17	16-18
Nb	5.1	5.1	5.17	4.91
Mo	4.2	3.06	3.1	3.18
Ti	0.9	0.94	0.89	0.97
Al	0.3	0.44	0.53	0.63
C	0.08	0.04	0.03	0.034
Co		0.27	0.17	
Si		0.12	0.08	
Ref.	[9]	[9]	[9]	ASM Standard

Mechanical Properties

In718 provides outstanding tensile and creep-rupture properties within a range of a temperature of up to 740 ºC. Beyond this temperature, IN718 alloy, as in the AORA system, may not provide the expected performance as the properties will lead to change due to very high temperature range [65]. Table 3 shows the material properties of IN718 at different temperatures [10].

Table 3

IN718-Mechanical Properties [1]

Test Temperature		0.2% Yield Strength		Tensile Strength		% Elongation 2"
°F	°C	ksi	MPa	ksi	MPa	
200	93	170	1172	204	1407	21.0
400	204	163	1124	198	1365	20.0
600	316	159	1096	195	1344	20.0
800	427	156	1076	191	1317	19.0
1000	538	155	1069	185	1276	18.0
1200	649	149	1027	168	1158	19.0
1400	760	110	758	110	758	27.0

Heat Treatment: 1 hr - 1800°F, air cool + 8 hr-1325°F, cool 100°F/hr to 1150°F, hold 8 hr, air cool.

Tensile Properties

Tensile test can determine the ultimate strength of IN718, such as yield strength, modulus of elasticity [66]. The type of material along with temperature, load, gauge length are the important variables for the Tensile properties [11]. Strain analysis as shown in Figure 4 case shows,

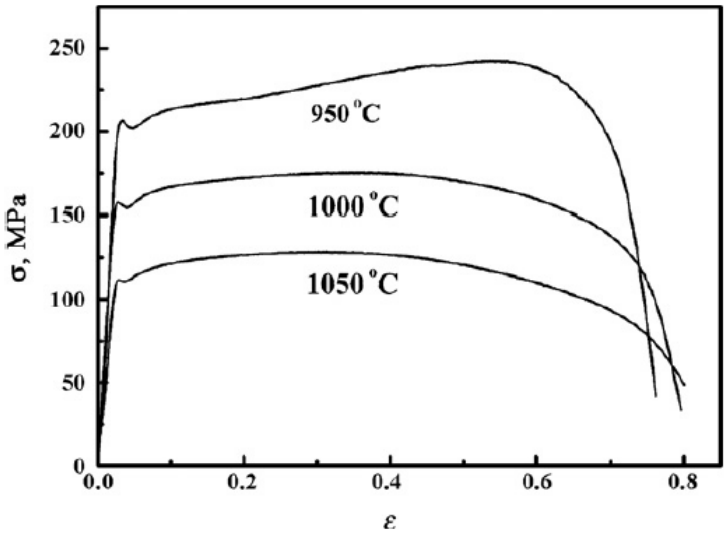

Figure 7: Tensile stress vs. strain curves for IN 718 [11]

Because of the flow localization and dynamic strain, the lower strain rate passes the oscillation rate [11].

Creep-Fatigue Properties

Research study at Ref. [26] represents creep-fatigue effect of a rim of IN 718. The Kartik-Vikas research procedure was implemented in this study [39]. Because the strain rate has reduced in the plastic strain, deformation dependent on time has generated in the lower contribution cycle, which is considered as creep. There are three modes to grow a crack, and they both can be creep and fatigue, that means it can be properties of additive, competitive, and interactive as shown in Figure 8.

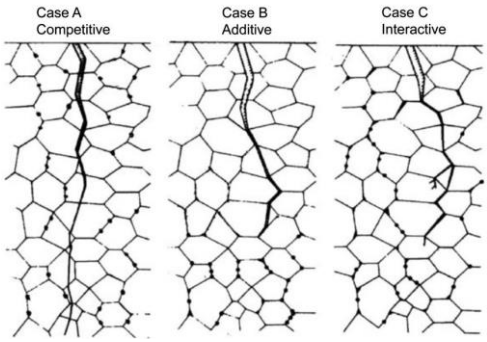

Figure 8: Crack growth cases [26]

Selective Laser Melting of IN718

In the SLM process of IN718 various grain structures can formed due to the different scanning strategies in this procedure, which provides an excellent possibility of modification of mechanical properties in any single part of the sample [67,68,69].

In the SLM process, the build orientation is considered a crucial part of the method [70]. Even there is impacts on the vertically and horizontally fabricated samples in a difference of 7% in their tensile properties or compressive strength between these two fabricated samples [71]. Increasing laser power leads to uniformly distributed dendrites from the clustered columnar dendrites. With the 330 j/m laser power 98% density of the sample was achieved [63, 72, 73]. Solution treatment of the samples provided a better mechanical performance and microstructure

characteristics than other fabrication methods [74]. Moreover, the elevated temperature in the solution treatment can enhance these mechanical and microstructural performances even better [75]. That is why Selective Laser Melted IN718 is more suitable in the application of Solar Absorber tube for the Concentrated Solar Power system.

IN718 with Boron

IN718 can withstand very high pressure up to 1000 psi and high temperatures such as 750°C [76, 77, 78]. However, IN718 being exposed constantly at high temperature, thermal decomposition observed while the IN718 melts, which leads to a deterioration of its porosity resistance and microhardness [79,80].

Reinforcement materials, like Boron-Nitride have become more popular due to its excellent thermo-mechanical properties [81,82]. A hexagonal Boron-Nitride nanosheet has a low density of 2.29 g/cm^3 and high elastic modulus of 700-900 GPa [28]. This nanosheet also has the ability to work as thermal shock barrier to prevent deformation at high temperature [81,83], which ultimately improves the wear behavior and enhances the friction resistance of a material [84,85,86].

SH Kim, GH Shin et el. [87] studied the thermos-mechanical improvement of IN718 where the research used the Laser Powder Bed Fusion (LPBF). The volume ratio of Boron-nitride ranged from 0-12% were printed using this technology. The SEM of the particles are shown below.

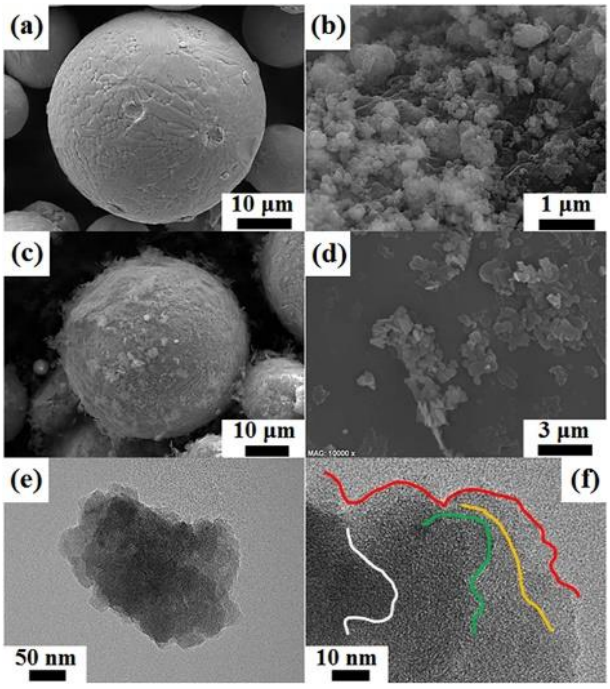

Figure 9: SEM analysis of Inconel718 and Boron-Nitride samples [87]

According to the temperature, IN718 phase transformation was studied, and the resistance of heat was obtained by the IN718 with Boron-Nitride as shown in Figure 9 [87].

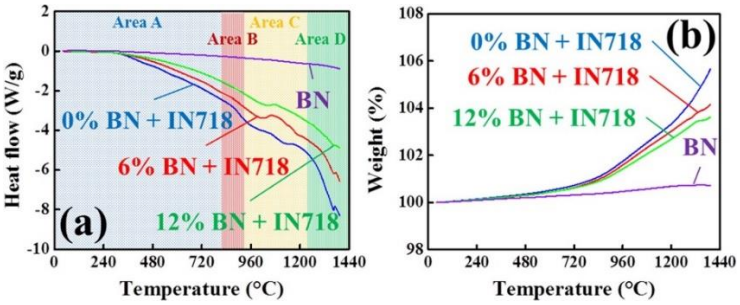

Figure 10: Heat resistance analysis of Inconel718 and Boron-Nitride composition [87]

The literature study [87] shows the BN with In718 increased the melting temperature peak to 1364^{o}C and increased the resistance of the thermal stress performance of composition drastically.

CHAPTER III

METHODOLOGY

Solar Absorber Tube with Internal Fin structure

Initial capability of the machine was checked to determine if the machine is capable of successfully fabricating the required thin wall for the solar absorber tube. The tubes without fin were designed with CAD software Autodesk fusion 360 in ‘stl’ format and the ‘stl’ file of the tube then transferred to the material magics software to generate the support structure and set the process parameter as well as the hatch strategy. Process parameters were set as the Renishaw default parameter and ‘chess’ hatch strategy was selected in the process. A combination of block and point support structure was generated. After support generation, the new complete ‘ready to print’ job file was sent to the Renishaw AM 250 SLM printer. Powder was fed to the powder feeder through the with through a nozzle without any kind of expose in the air to avoid oxidation. And built chamber was filled with Argon gas by replacing the Oxygen gas inside the chamber to create the inert gas environment. When the oxygen level reached 500 ppm (parts per million), printing procedure started immediately layer by layer. Two tubes without any internal fin structure were printed successfully as shown in figure 11, where the tube length is 60mm with a diameter of 20mm and the wall thickness is 0.75mm, which is a thin wall for solar absorber tube.

Figure 11: Tubes without fin structure

Two different internal fin structures were designed by the project collaborator University of Arizona (UoA) team to test the heat-transfer performance. Multi-head helical fin and continuous helical fin as shown in figure 12.

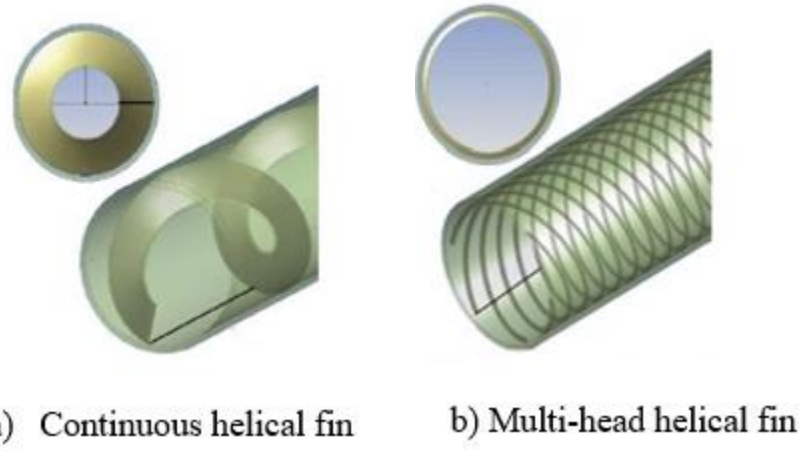

Figure 12: Design of Internal Fin Structure [Project collaborator team-UoA]

The multi-head helical fin, and continuous helical fin designs were fabricated with EOS M 290 3D printer. 12 sections of tubes (109.41 mm each) from each design were printed, so that the length of the Solar absorber tube for the solar-thermal power plant can reach 1.31m for the heat-transfer testing and the fully developed flow can be reached within the 1.31m long test section. As per the simulation and design, it was important to fabricate each 3D printed tube section with full

rotates. Each rotate is a full pitch for the internal fin, determined by the simulation analysis.

The tubes with two different fin structures were designed with CAD software Solidworks in ‘stl’ format and the file transferred to the Material Magics Software for support generation as shown in Figure 13. The support was generated manually for the overhung internal fin structure, material magics software creates support throughout the tube to support the overhung structure. It would be difficult to separate the support completely throughout the fin structure within this small tube diameter, hence it would damage the fin design with the existing support structure. To provide enough strength to the overhung internal fun structure, a combination of block and point support was generated as shown in figure 13.

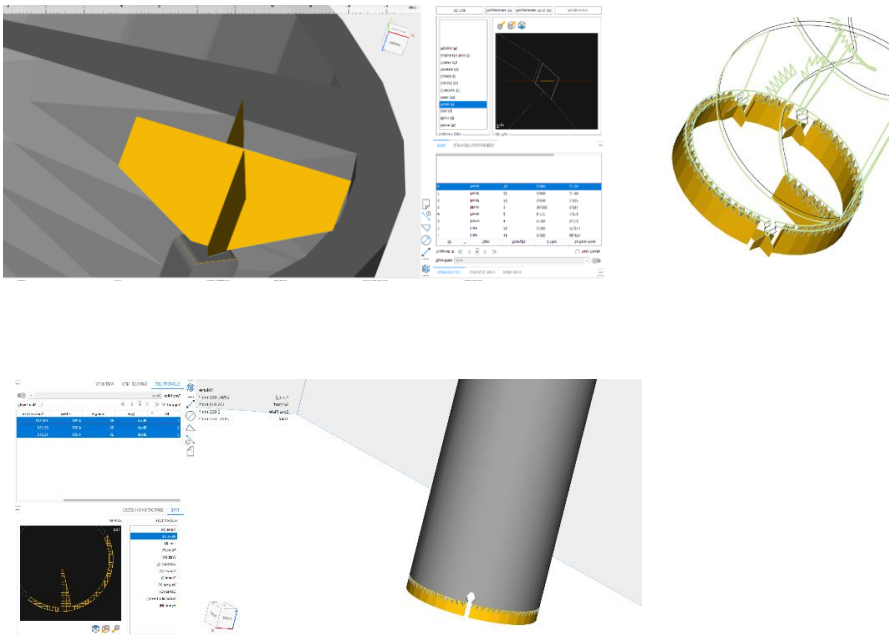

Figure 13: Support generation of the tube with internal fin structure

After generating the support, the file transferred to the EOS software to prepare the job file by positioning on the software build plate which is the exact dimension for the machine build plate as shown in Figure 14.

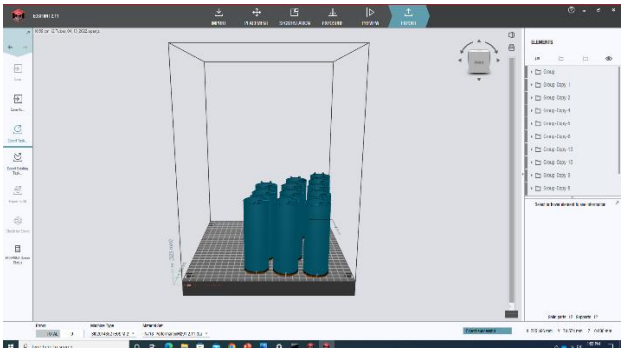

Figure 14: Printing job preparation with EOSPRINT 2.11 software

Parameter sets were selected for IN718, and Laser Scanning direction was selected ‘against flow’ to make sure inert gas flow is not in the way of the laser. The absorber tubes with these two designs were successfully fabricated with EOS M 290 machine as shown in Figure 15 & Figure 16.

Figure 15: Larger section of tubes with Continuous helical fin structure

Figure 16: larger section of the tubes with multi-head and continuous helical fins

Table 4

Dimension of the Tube:

Tube Dimension	Unit (mm)
Tube Segment	35.3X3
Tube Height	105.9
Support Structure	5
Total build height	110.9
Inner Diameter, Di	35.3
Outer Diameter, Do	36.7
Tube Thickness	1.4
Fin Thickness	1.4

Table 5

Default Laser Parameter for In718 for EOS M 290

Laser Process Parameter	Main Part	Support Structure Part
Laser Power	285 W	100 W
Laser Speed	960 mm/s	900 mm/s
Hatch Distance	0.11 mm	0.04 mm
Layer Thickness	40 um	40 um
Laser Energy	67.47 j/mm3	2.78 j/mm3

Fabrication of samples with B and IN718

This research analyzes the effect of B with IN718 to enhance the optical and thermal properties of absorber tube, and to determine the optimized laser parameters for better performance.

Powder Mixing

The powder was mixed in the Argon-filled, oxygen-free environment, called Glove Box is shown in figure 15. 3% B, 1% B, and 0.5% B was mixed with Inconel 718. Then the angle of repose method was done to check the flowability of each mixture, shown in figure 17.

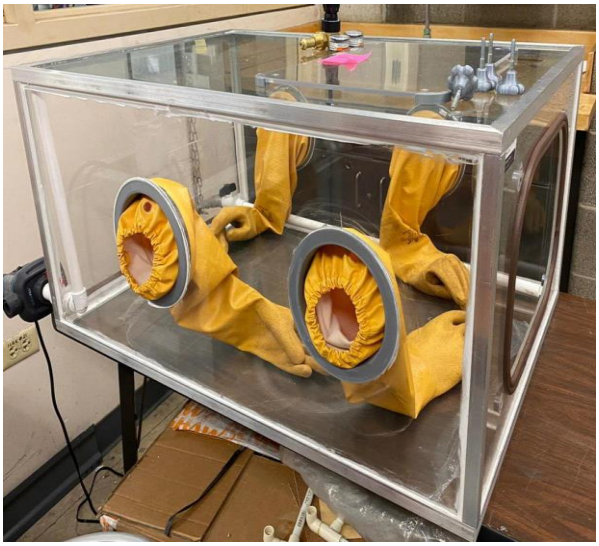

Figure 17: Argon filled Glove Box

From the Angle of Repose (AOR) method, figure 18(a) indicates the angle is 42.43 for 3% B mixture, Figure 18(b) indicates the angle of 41.25 for 1% B mixture, and figure 18(c) indicates the angle of 37.68 for 0.5% B mixture. Table 4 shows the relation between the angle and the flowability.

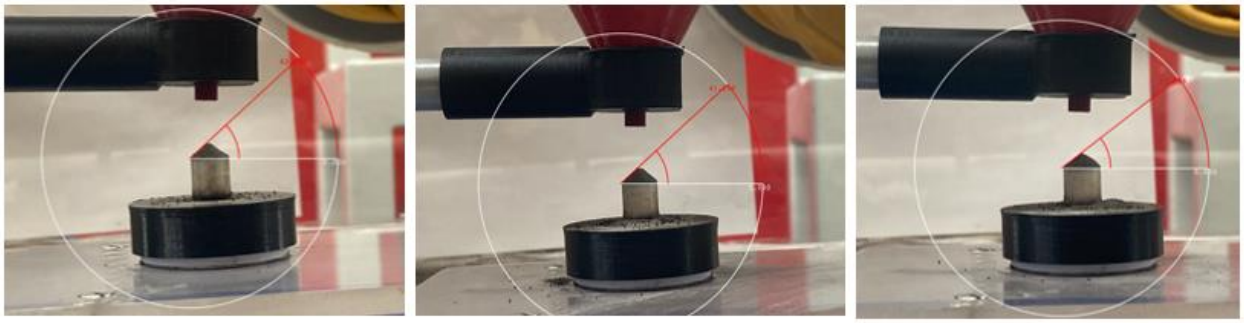

(a): AOR 42.439 for 3% B mixture (b): AOR 41.25 for 1% B mixture (c): AOR for 0.5% B mixture

Figure 18: AOR for 3%, 1%, and 0.5% B with IN718 mixture

Table 6

Relation Between the angle and the flowability

Angle	Flowability
≤30°	Good Flowability
30°-45°	Some Cohesiveness
45°-55°	True Cohesiveness
≥55°	Limited Cohesiveness

From the flowability chart, it is clear that 3% B with IN718 provides the least flowability. So, powder was mixed in larger quantities for sample fabrication with 0.5% and 1% B with IN718 using a V-shape mixture with low rpm for 8 hours as projecting in Figure 19.

Figure 19: B with IN718 powder mixing in the V-shape mixture

Figure 20: 1500 gm 1% B mixture and 1500 gm 0.5% B mixture

SEM of Materials

After mixing the powder, to identify the uniformity of the mixed powder, Scanning Electron Microscopic (SEM) analysis was conducted for pure IN718, pure Boron powder, 0.5% B with IN718, 1% B with IN718, and 3% B with IN718 as shown in figures below. Where the SEM analysis shows IN718 is spherical shaped, which provides a better flowability, where B is highly agglomerated. Also, 0.5% B with IN718 ensures the better mixing quality hence better flowability, while 1% and 3% B with IN718 mixture contains agglomerated B particles some of them are not even attached to the IN718 particles.

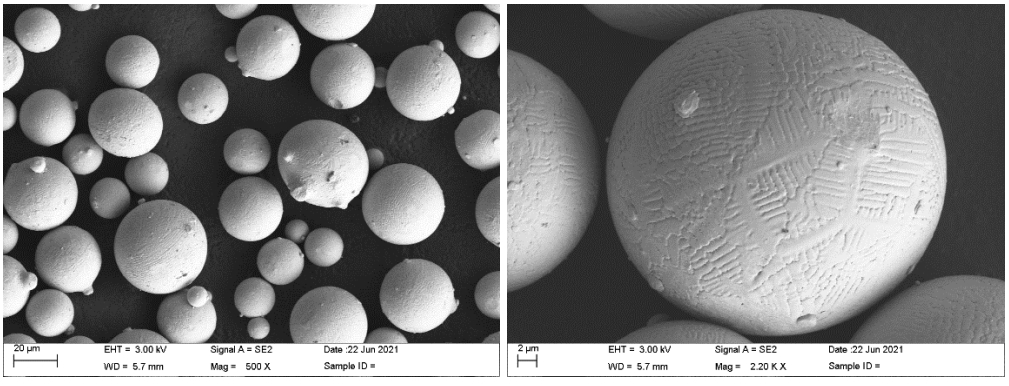

Figure 21: SEM analysis of IN718

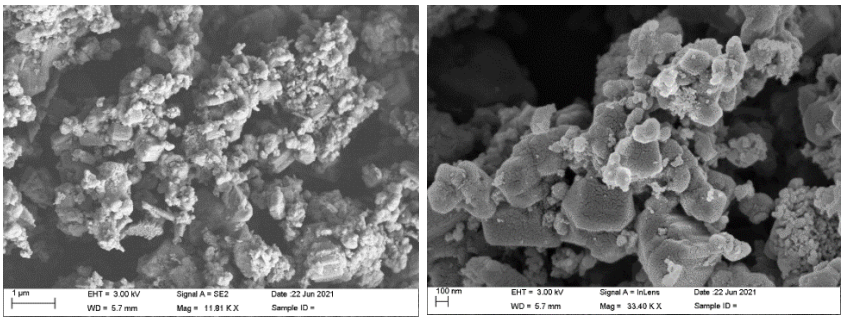

Figure 22: SEM analysis of Boron

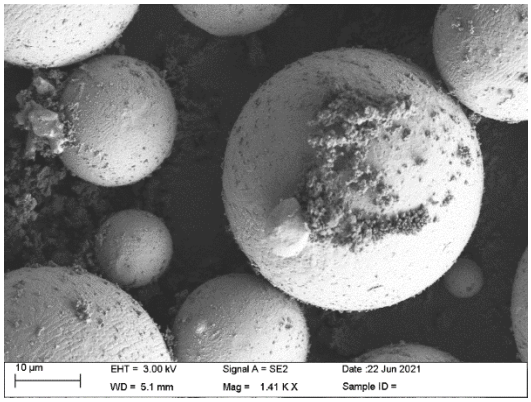

Figure 23: SEM analysis of 3% B with IN71

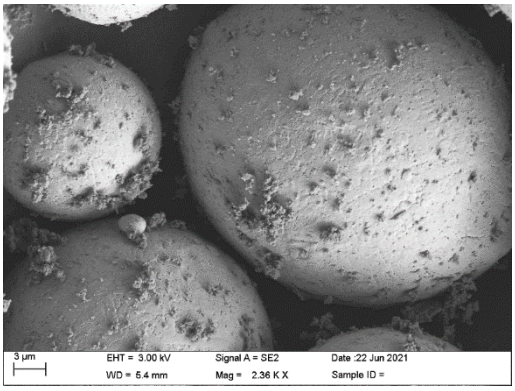

Figure 24: SEM analysis of 1% B with IN718

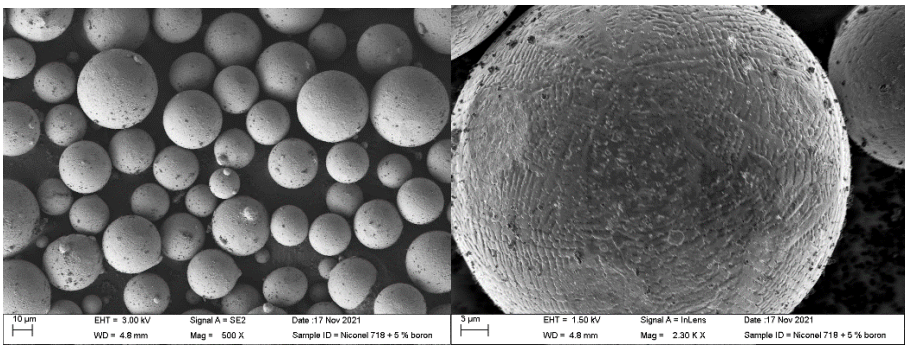

Figure 25: SEM analysis of 0.5% B with IN718

AM Fabrication

After mixing the powder, to determine how different printing parameters affect the microstructure of the mixture of Inconel718 with 0.5% and 1% of B, two separate 3 × 3 test series were created with materials magic software. The laser power, P was set at 200 W, and Point distance, PD=55µm; Exposure Time, ET was set at 80,88, and 96 µS; hatch distance, HD was set at 70,80, and 90 µm and Layer Thickness 60 µm as mentioned in Table 7. Each sample of the 3X3 test matrix was fabricated up to 20 layers with the Renishaw AM400 Reduced Build Volume (RBV) system.

The first step of the SLM procedure was pouring the material into the powder feeder and leveling the build plate and confirming the layer thickness by running the powder flowability two to three times. The oxygen level was set at 500 ppm. The laser started scanning when the oxygen level reached that range, and the chamber was filled with the inert gas Argon. The samples were printed layer by layer until they reached the input build height.

Table 7

Parameter settings for 3X3 test

Run	Power (w)	Hatch Distance(µm)	Point Distance (µm)	ExposureTime (µS)	Layer Thickness (µm)	Energy Density (j/mm3)
A1	200	90	55	80	60	53.87
A2	200	90	55	88	60	59.25
A3	200	90	55	96	60	64.64
B1	200	80	55	80	60	60.60
B2	200	80	55	88	60	66.66
B3	200	80	55	96	60	72.72
C1	200	70	55	80	60	69.26
C2	200	70	55	88	60	76.19
C3	200	70	55	96	60	83.11

Table 8

Energy Density of the samples

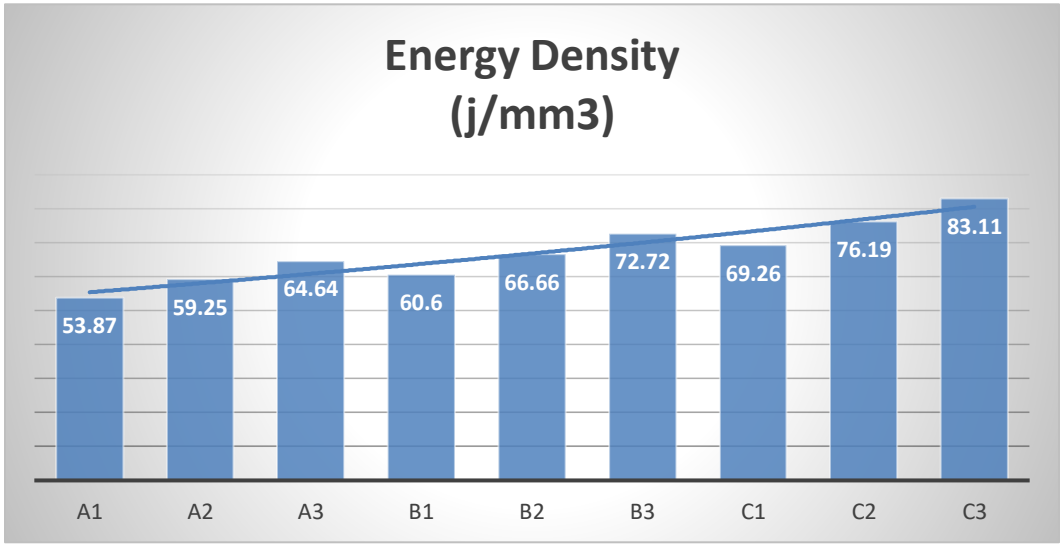

Figure 26: 3X3 test series for 1% B mixture

Figure 27: 3x3 test series for 0.5% B mixture

Cubic material samples with 0.5% Boron and 1% Boron were fabricated on a Reduced Build Volume in Renishaw AM 400 machine. A powder flowability test was conducted to ensure powder deposition using recoater blade. 1% and 0.5% Boron mixture were selected to produce 3X3 test matrices for different process parameters. When varying the process parameters, 120 μm hatch distance (HD), 200 W laser power (P), 55 μm point distance (PD), and 80 μs exposure time (ET) were used as the base values. In the test matrices, HD was set at (70,80,90), ET was set at (80, 88,96) (shown in Table 5). Default wiper speed caused uneven powder deposition, with less

amount of powder at the front end of the substrate (at the end of recoater blade movement. This caused warping of layers at certain samples due to lack of powder and excessive heat. We rearranged the sample layout and slowed down the moving speed for better results, as shown in Figure 21. Microscopic analysis was carried out to examine the as-built samples. For 1% Boron cubic samples, cracks between layers can was observed, and the size of the crack ranges between 200-500μm, as shown in Figure 28. No cracks were identified on samples using 0.5% Boron as shown in Figure 29; therefore, the rest of the analysis is based on the 0.5% Boron mixture samples.

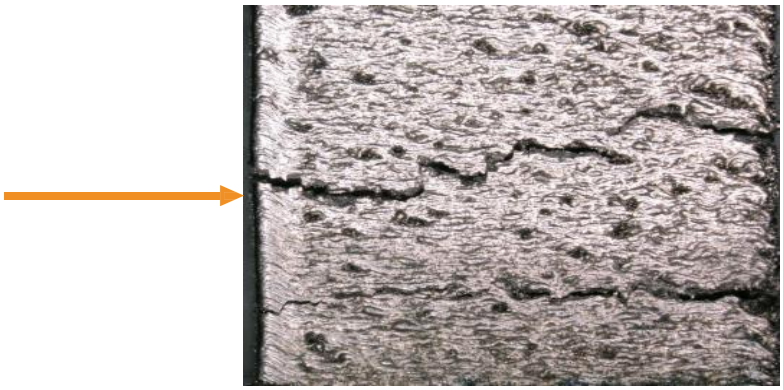

Figure 28: 1 wt% B with IN718 sample

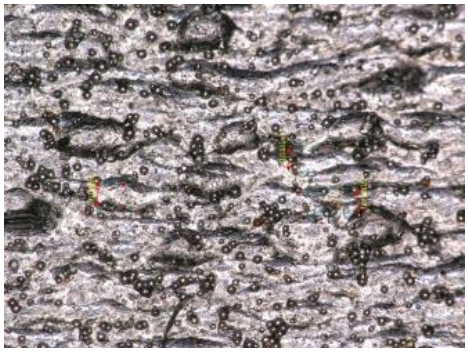

Figure 29: 0.5 wt% B with IN718 sample

CHAPTER IV

RESULTS AND FINDINGS

Surface Morphology of the Solar Absorber Tube

The first part of this work regards the challenges of fabrication of Solar Absorber tube with different internal fin structure in a large section to achieve a combine length of 1m. Moreover, the design with internal fin structures was a challenge and almost impossible to achieve in conventional method. Also, 3D printing of overhung structure with higher length, generates internal support structures which are not easy to remove after printing the parts and achieving a uniform finish on overall fin structure. To avoid this problem, automatically generated support structures around the fins were removed and a combination of block and point support structures were created to provide extra strength and it was selected to be followed in this work.

Figure 30: Solar absorber tube with internal fin structure

After successfully printing the tubes with Selective Laser Melting 3D Printing Procedure, the tubes were sent to the University of Arizona and ready for heat transfer for Solar Absorber Tube.

Surface Roughness of Tubes

Literature survey proves that increasing the surface roughness will increase the light trapping by enhancing absorbance and decreasing reflectivity [32, 33, 34] as Shown in Table 9 [32].

Table 9

Results for Reflectance and absorptance [32]

Type	Surface finish	Reflectance ρ_S [%]	Absorptance α_S [%]
Inconel 718	with	53	47
Inconel 718	without	46	54
CrCo	with	60	40
CrCo	without	31	69

The absorbance of a material increases with rougher surfaces due to the light trapping capabilities of the peaks and valleys of the surface.

To provide the concept, surface roughness of the short solar absorber tubes was measured using microscope and surface profilometer. A little portion of the tube was cut open and separated. After that the inner and outer surface roughness were measured using a surface profilometer. The average surface roughness for the 3D printed IN718 tube is about 9~10 μm as shown in figure 31.

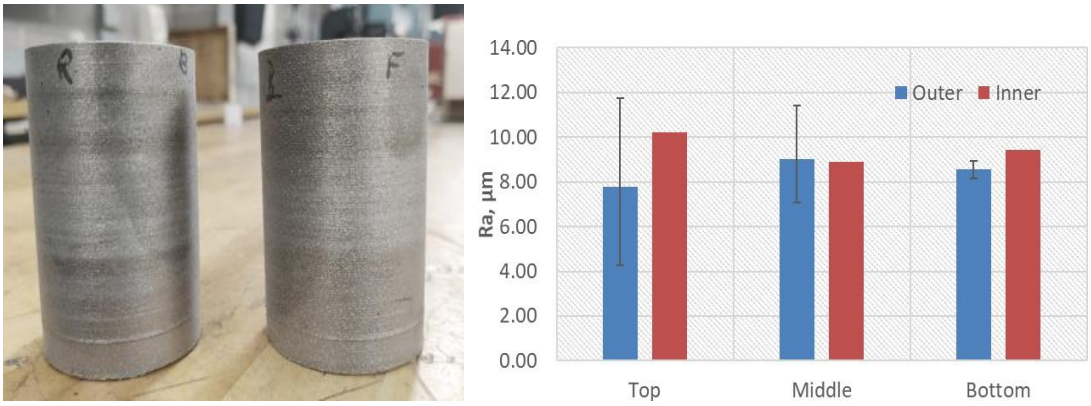

Figure 31: Surface roughness measurement using Surface Profilometer

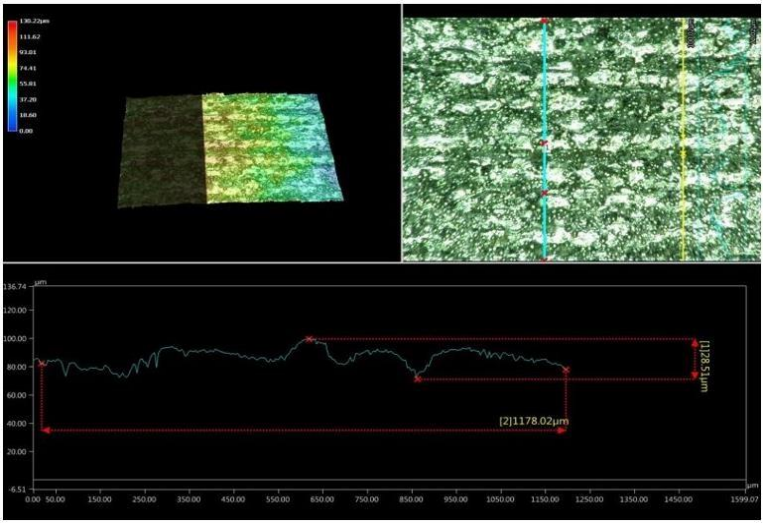

Figure 32: Surface roughness measurement using microscope

Microscopic Analysis Results of Printed Samples

Only the 0.5% Boron mixture samples were cut open and polished for further microscopic analysis, as shown in Figure 33.

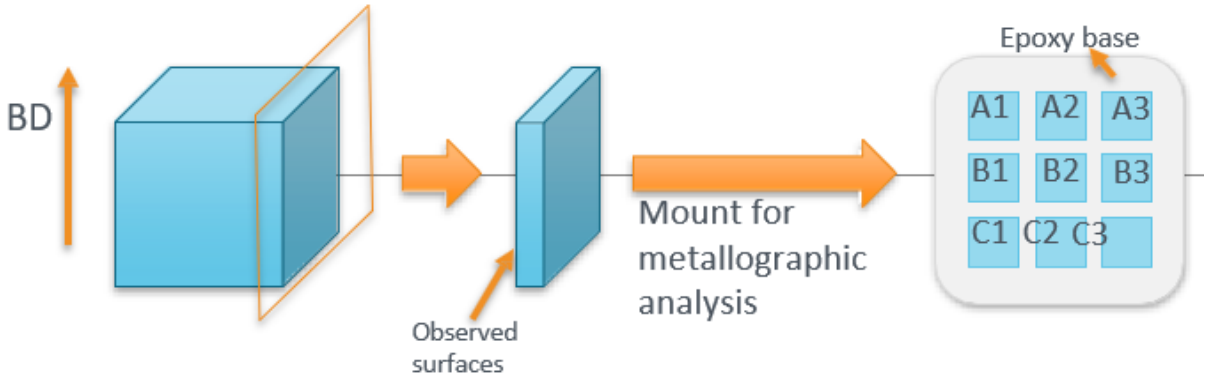

Figure 33: Sample mounting for metallographic analysis

Black spots were observed in all 9 samples, where the spherical-shaped black spots were identified as pores, and they generated during additive manufacturing process. The irregular spots that typically appear as short needles and nearly equilateral polygonal, they are smaller than the size of pores and uniformly distributed in the matrix. They are inferred to be secondary phases containing boride. Sample A1 shows containing the least black spots and the size of irregular shaped black spots are also observed smallest at Sample A1. The size of these particles is measured with the ImageJ software as shown in figure 35. Where sample A1 was observed the lowest average particle size of 101.14 nm, and sample C2 was observed the highest average particle size 404.611 nm.

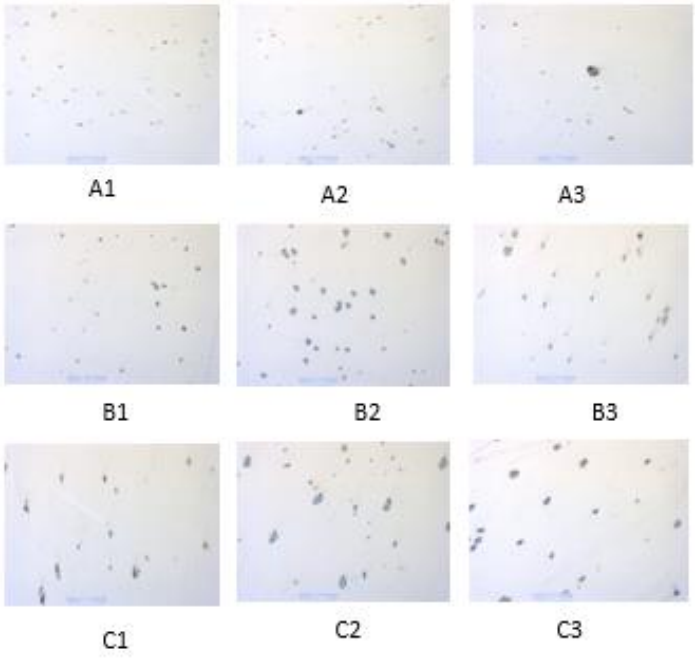

Figure 34: Optical microscopic analysis of samples

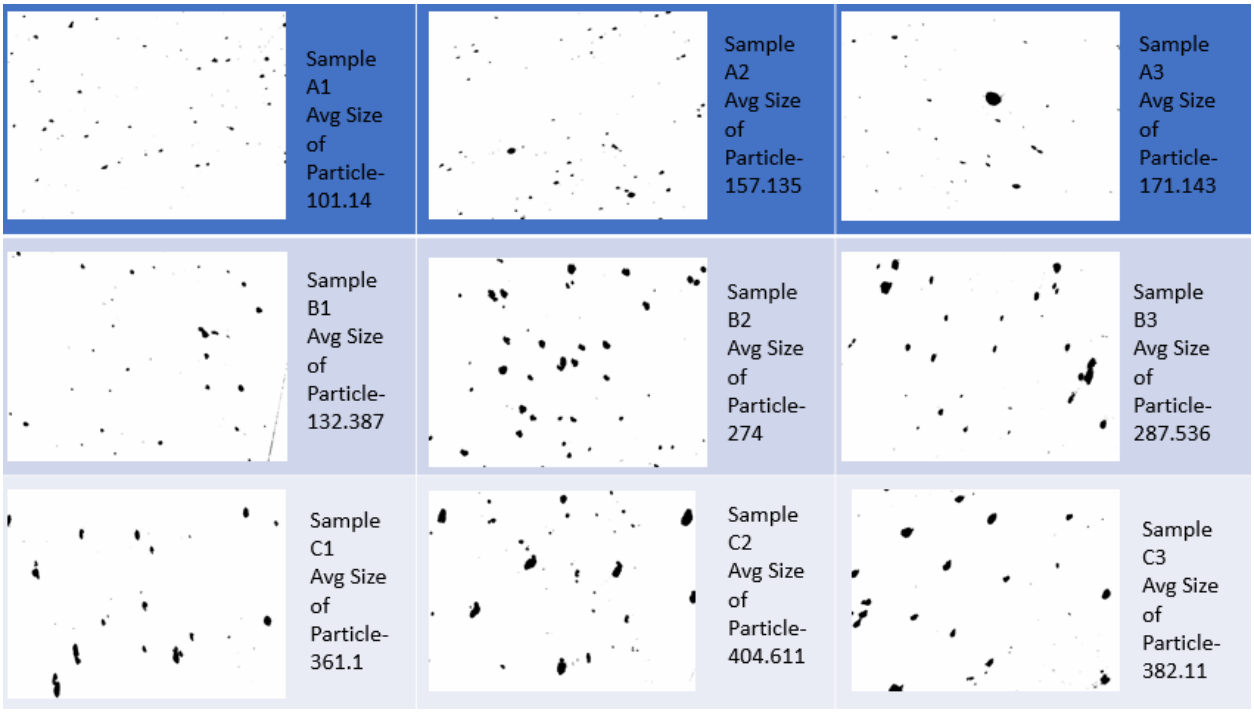

Figure 35: ImageJ particle size analysis of the samples

Table 10

Summary of ImageJ analysis:

Slice	Count	Total Area	Average Size	%Area	Mean
A1.jpg	50	5057	101.14	0.655	255
A2.jpg	52	8171	157.135	0.505	255
A3.jpg	21	3594	171.143	0.552	255
B1.jpg	31	4104	132.387	0.582	255
B2.jpg	44	12056	274	1.921	255
B3.jpg	28	10851	387.536	1.439	255
C1.jpg	20	7222	361.1	1.237	252.98
C2.jpg	36	14566	404.611	1.903	255
C3.jpg	27	10317	382.111	1.652	254.9

Table 11

Relation between Energy density and average particle/porosity size:

Sample	Energy Density	Average Size
A1	53.87	101.14
A2	59.25	157.135
B1	60.6	132.387
A3	64.64	171.143
B2	66.66	274
C1	69.26	361.1
B3	72.72	387.536
C2	76.19	404.611
C3	83.11	382.111

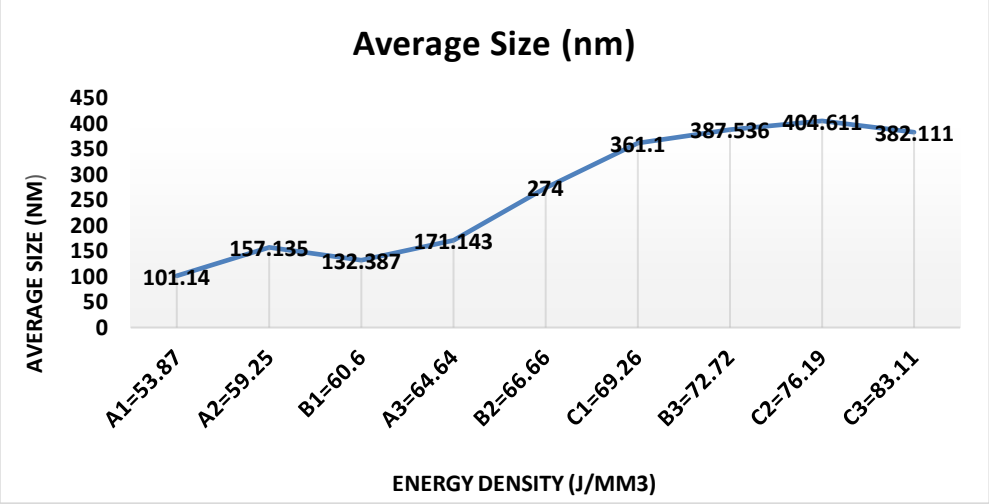

Figure 36: Average size vs Energy Density shows a linear upward trend.

The plot above in figure 36 laser energy density has effect on average over-melted particles and porous particles. From the optical microscope and ImageJ analysis, sample A1 has the lowest average size of particles with the lowest energy density, which is considered the best performance among all. In the correlation chart, it is clearly observed that with increasing amount of Laser induced Energy Density, the over-melted particles are also increasing exponentially.

SEM and EDS analysis of the Printed samples

SEM analysis of the printed samples was conducted. The existence of un-melted, over-melted, and porous IN718 and B particles were observed in the SEM images as shown in figure 37. Low energy density is unable to generate enough energy to melt all the particles in the laser melting process, which causes un-melted particles of the material as shown in Figure 37(a). Due to the heat generation in the laser melting process, higher energy density may induce a higher temperature at the sample parts, causing over-melting of the material as shown in figure 37(b). Some porosities were also observed in the sample parts as shown in figure 37(c).

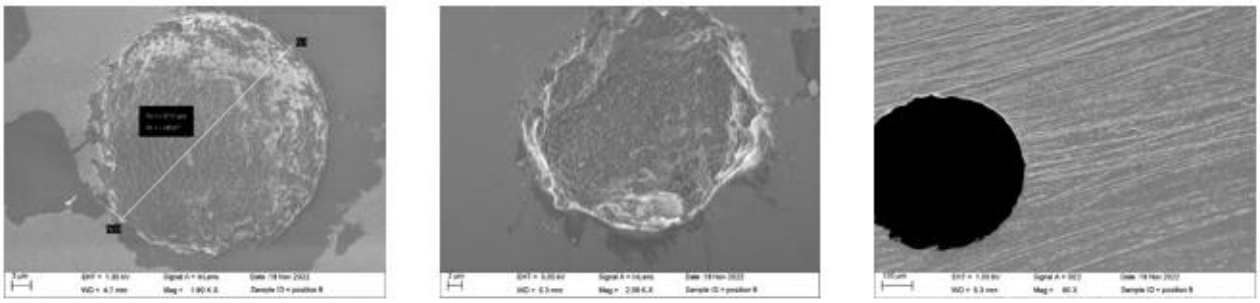

a) Un-melted Particle b) Over-melted particles c) Porous Particle

Figure 37: SEM analysis of 0.5% B with IN718 samples

EDS analysis of the sample was conducted to ensure the existence of the IN718 components and Boron particles as shown in figure 38.

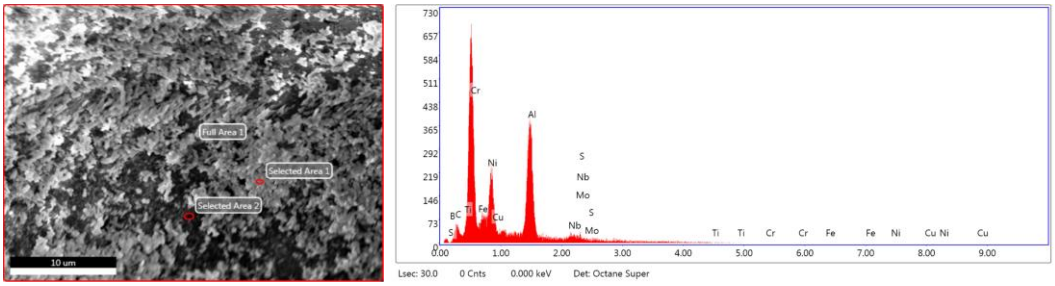

eZAF Smart Quant Results

Element	Weight %	Atomic %	Net Int.	Error %	Kratio	Z	A	F
B K	0.03	0.11	0.03	99.99	0.0001	1.3410	0.2995	1.0000
C K	4.21	13.15	31.09	14.38	0.0299	1.3917	0.5099	1.0000
TiL	13.65	10.68	13.54	17.05	0.1268	0.9466	0.9814	1.0000
CrL	38.39	27.68	120.56	6.42	0.3163	0.9340	0.8821	1.0000
FeL	0.39	0.26	1.54	85.79	0.0027	0.9266	0.7409	1.0000
NiL	12.75	8.14	69.16	9.38	0.1026	0.9350	0.8612	1.0000
CuL	0.00	0.00	0.02	99.99	0.0000	0.8877	0.8364	1.0000
AlK	28.03	38.95	247.97	7.79	0.2875	1.1251	0.9106	1.0010
NbL	1.67	0.67	3.51	83.85	0.0128	0.7787	0.9837	0.9996
MoL	0.87	0.34	1.61	95.42	0.0066	0.7641	0.9896	0.9996
S K	0.01	0.01	0.03	99.99	0.0001	1.1119	0.9615	1.0042

Figure 38: EDS analysis of printed sample

The EDS analysis shows the sample contains the components of IN718 and a little percentage of Boron as well. Which indicates there was no other material contaminated during the process. Also, the components of IN718 and B remain the same after Selective Laser Melting Procedure as expected.

Reflectance of Printed samples with IN718 and Boron

According to Kirchhoff's Law [35] in radiation, the spectral absorptivity α, reflectivity ρ and emissivity ε has the following relations:

Thermal Radiation Equation:

$\alpha + \rho = 1$

Kirchhoff's Law:

$\alpha = \varepsilon$

The absorptivity and emissivity test of the 9 cubic printed samples of IN718 with 0.5% B with different laser parameters were conducted by the project collaborator University of Arizona team. Different ranges of wavelength were approached at room temperature to obtain the hemispherical reflectance of the samples. Most of the samples have a reflectance of less than 25% in the visible light range, which corresponds to an emissivity of ~75%. Once entering the infrared regime, the emissivity drops to approximately 60% for most of the samples. The absorptivity of these 0.5% Boron mixture can reach 80% around 3μm, where the emissivity is around 55% in the visible light range (400um-700um). These tests were performed at a room temperature so we assume some differences will occur when elevated to the operating temperature range. Literature shows that emissivity increases with temperature from 0.24 to 0.33 having as-received conditions with a temperature range of 200-1000˚C [36].

CHAPTER V

CONCLUSION AND FUTURE DIRECTIONS

The first part of this work regards the challenges of fabrication of Solar Absorber tube with different internal fin structure in a large section to achieve a combine length of 1 m. Moreover, the design with internal fin structures was a challenge and almost impossible to achieve in conventional method to have a uniform structure throughout the fin. Also, 3D printing of overhung structure with higher length, requires internal support structures which are not easy to remove after printing the parts and achieving a uniform finish on overall fin structure. To avoid this problem, automatically generated support structures around the fins were removed and a combination of block and point support structures were created to provide extra strength and it was selected to be followed in this work. Fabrication of the larger section of the tube with thin wall and overhung structure needs special support generation.

The second part of this thesis was to determine the effect of Boron with IN718 to improve the optical-thermal properties of solar absorber tube. 0.5 % and 1% B were mixed with IN718 and fabricated with Selective Laser Melting 3D printing technology. Cubic samples were successfully printed based on powder mixture with 0.5% B and 99.5% IN718, using 9 different parameters to obtain the optimistic result for the absorber tube. 1% B samples did not print successfully. So, the optical microscopic and reflectance analysis was conducted for 0.5% B samples only. Where sample A1 showed comparatively better results than all other printed samples for both optical microscopic analysis and reflectance analysis. The parameters for sample A1- Laser power = 200 w, Hatch distance = 0.09 um, Point Distance = 55 um, Exposure time = 80 us and the Layer

thickness is 60 um.

Optical microscopic analysis showed evidence of un-melted particles, which was considered as a challenge to melt all the particles properly without over melting the samples hence result in overburn and distortion of the samples. Future study is needed to fabricate the samples with IN718 and B to melt all the particles properly in the selective Laser melting procedure to observe if that can improve any efficiency.

Adding 0.5% B to the IN718 increased the solar absorptivity and decreased the emissivity. Increased percentage of B such as 1%, 3% with IN718 will need to be study to increase the effectiveness of optical-thermal properties of solar absorber tube.

REFERENCES

1. Pinkerton, A.J., and Li, L., 2004, "Modelling the geometry of a moving laser melt pool and deposition track via energy and mass balances," Journal of Physics D: Applied Physics, 37(14), pp. 1885-1895.

2. P.J. Blau, “Erosion/Corrosion," in ASM Handbook, Volume 18 - Friction, Lubrication, and Wear Technology, ASM International, 1992, pp. 199–213.

3. M. Liu et al., “Review on concentrating solar power plants and new developments in high temperature thermal energy storage technologies," Renew. Sustain. Energy Rev., vol. 53, pp. 1411–1432, 2016.

4. Shenoy S., Peralta P., Solanki K., Sieradzki K., "Effect of Foreign Object Damage on Fatigue of Inconel 718 at Elevated Temperature (1050 ºC)," Arizona state univ.,pp. 75-78, pp. 1411–1432, 2016.

5. Wang, Z., Guan, K., Gao, M., Li, X., Chen, X., and Zeng, X., 2012, "The microstructure and mechanical properties of deposited-IN718 by selective laser melting," Journal of Alloys and Compounds, 513(0), pp. 518-523.

6. Qi, H., Azer, M., and Ritter, A., 2009, "Studies of Standard Heat Treatment Effects on Microstructure and Mechanical Properties of Laser Net Shape Manufactured INCONEL 718," Metal and Mat Trans A, 40(10), pp. 2410-2422.

7. Parimi, L. L., Clark, D., and Attallah, M. M., 2014, "Microstructural and texture development in direct laser fabricated IN718," Materials Characterization, 89, pp. 102-111.

8. Qi, H., Azer, M., and Ritter, A., 2009, "Studies of Standard Heat Treatment Effects on Microstructure and Mechanical Properties of Laser Net Shape Manufactured INCONEL 718," Metal and Mat Trans A, 40(10), pp. 2410-2422.

9. Parimi, L. L., Clark, D., and Attallah, M. M., 2014, "Microstructural and texture development in direct laser fabricated IN718," Materials Characterization, 89, pp. 102-111.

10. Gu, D.D., et al., Laser additive manufacturing of metallic components: materials, processes and mechanisms. International materials reviews, 2012. 57(3): p. 133-164.

11. Rao, H., et al., The influence of processing parameters on Aluminum alloy A357 manufactured by Selective Laser Melting. Materials & Design, 2016. 109: p. 334-346.

12. Zhou, L., et al., Selective laser melting of pure tantalum: densification, microstructure and mechanical behaviors. Materials Science and Engineering: A, 2017. 707: p. 443-451.

13. Lu, Y., et al., Study on the microstructure, mechanical property and residual stress of SLM Inconel-718 alloy manufactured by differing island scanning strategy. Optics & Laser Technology, 2015. 75: p. 197-206.

14. Zou, S., et al., Numerical analysis of the effect of the scan strategy on the residual stress in the multi-laser selective laser melting. Results in Physics, 2020. 16: p. 103005

15. Dong, Z., et al., effect of hatch spacing on melt pool and as-built quality during selective laser melting of stainless steel: Modeling and experimental approaches. Materials, 2019. 12(1): p. 50.

16. Pupo, Y., et al., Scanning space analysis in selective laser melting for CoCrMo powder. Procedia Engineering, 2013. 63: p. 370-378.

17. Aboulkhair, N.T., et al., Reducing porosity in AlSi10Mg parts processed by selective laser melting. Additive manufacturing, 2014. 1: p. 77-86.

18. Liu, Ming, et al. "Review on concentrating solar power plants and new developments in high temperature thermal energy storage technologies." *Renewable and Sustainable Energy Reviews* 53 (2016): 1411-1432.

19. Palacios, A., et al. "Thermal energy storage technologies for concentrated solar power–A review from a materials perspective." *Renewable Energy* 156 (2020): 1244-1265.

20. Islam, Md Tasbirul, et al. "A comprehensive review of state-of-the-art concentrating solar power (CSP) technologies: Current status and research trends." *Renewable and Sustainable Energy Reviews* 91 (2018): 987-1018.

21. Yellowhair, Julius ;Ho, Clifford K. ; Ortega, Jesus D. ;Christian, Joshua M. ;Andraka, Charles E. “Testing and optical modeling of novel concentrating solar receiver geometries to increase light trapping and effective solar absorptance”

22. Benoit, H., et al. "Review of heat transfer fluids in tube-receivers used in concentrating solar thermal systems: Properties and heat transfer coefficients." *Renewable and Sustainable Energy Reviews* 55 (2016): 298-315.

23. C.K. Ho, B.D. Iverson Review of high-temperature central receiver designs for concentrating solar power Renew Sustain Energy Rev, 29 (2014), pp. 835-846

24. Chicos, Lucia-Antoneta, et al. "Effect of concentrated solar energy on microstructure evolution of selective laser melted Ti-6Al-4V alloy." *The International Journal of Advanced Manufacturing Technology* 118.9 (2022): 3183-3207.

25. Kim, Yong, and Taebeom Seo. "Thermal performances comparisons of the glass evacuated tube solar collectors with shapes of absorber tube." *Renewable Energy* 32.5 (2007): 772-795.

26. Pal, Ram Kumar, and Ravi Kumar. "Investigations of thermo-hydrodynamics, structural stability, and thermal energy storage for direct steam generation in parabolic trough solar collector: A comprehensive review." *Journal of Cleaner Production* 311 (2021): 127550.

27. Kalogirou, Soteris A. "Solar thermal collectors and applications." *Progress in energy and combustion science* 30.3 (2004): 231-295.

28. Balaji, K., S. Iniyan, and V. Muthusamyswami. "Experimental investigation on heat transfer and pumping power of forced circulation flat plate solar collector using heat transfer enhancer in absorber tube." *Applied Thermal Engineering* 112 (2017): 237-247.

29. C. Soares, Microturbines: Applications for Distributed Energy Systems. Elsevier Science, 2011.

30. Malnieks, K., et al. "Black enamel for concentrated solar-power receivers." *Ceramics International* 40.8 (2014): 13321-13327.

31. Moutinho, Helio R., et al. "Adhesion mechanisms on solar glass: Effects of relative humidity, surface roughness, and particle shape and size." *Solar Energy Materials and Solar Cells* 172 (2017): 145-153.

32. Sallaberry, F., et al. "Towards standard testing materials for high temperature solar receivers." *Energy Procedia* 69 (2015): 532-542.

33. Zaversky, Fritz, et al. "Innovative and advanced materials research for high temperature solar receivers." *International Solar Energy Society Conference Proceedings*. 2014.

34. Hermoso, JL Navarro, and N. Martinez Sanz. "Receiver tube performance depending on cleaning methods." *Energy Procedia* 69 (2015): 1529-1539.

35. Ghanekar, Alok, et al. "Violation of Kirchhoff's Law of Thermal Radiation with Space–Time Modulated Grating." *ACS Photonics* 9.4 (2022): 1157-1164.

36. Greffet, Jean-Jacques, et al. "Generalized kirchhoff law." *arXiv preprint arXiv:1601.00312* (2016).

37. Laporte-Azcué, Marta, et al. "Material selection for solar central receiver tubes." *Solar Energy Materials and Solar Cells* 231 (2021): 111317.

38. R.Z. Wang, X.C. Zhang, J.G. Gong, X.M. Zhu, S.T. Tu, C.C. ZhangCreep-fatigue life prediction and interaction diagram in nickel-based GH4169 superalloy at 650 °C based on cycle-by-cycle concept Int. J. Fatig., 97 (2017), pp. 114-123.

39. Prasad, Kartik, et al. "Simultaneous creep–fatigue damage accumulation of forged turbine disc of IN 718 superalloy." *Materials Science and Engineering: A* 572 (2013): 1-7.

40. Special Metals Corp; INCONEL alloy 625, Spec. Met. Datasheets., 625 (2013), pp. 1-28

41. G. Augsburger, D. Favrat Modelling of the receiver transient flux distribution due to cloud passages on a solar tower thermal power plant
    Sol. Energy, 87 (2013), pp. 42-52

42. F.J. Collado Quick evaluation of the annual heliostat field efficiency Sol. Energy, 82 (2008), pp. 379-384.

43. M.R. Rodríguez-Sánchez, C. Marugan-Cruz, A. Acosta-Iborra, D. Santana Comparison of simplified heat transfer models and CFD simulations for molten salt external receiver Appl. Therm. Eng., 73 (2014), pp. 991-1003.

44. M. Laporte-Azcué, P.Á. González-Gómez, M.R. Rodríguez-Sánchez, D. Santana Deflection and stresses in solar central receivers Sol. Energy, 195 (2020), pp. 355-368

45. L.G. Radosevich, A.C. Skinrood The power production operation of solar one, the 10 MWe solar thermal central receiver pilot plant J. Sol. Energy Eng., 111 (1989), pp. 144-151.

46. D.R. Eno, G.A. Young, T.-L. Sham, A unified view of engineering creep parameters, in: ASME (Ed.), ASME Press. Vessel. Pip. Div. Conf. (PVP2008), Chicago, July 27-31, ASME, Chicago, 2008: pp. 777–792.

47. B.C. Du, Y.L. He, Z.J. Zheng, Z.D. Cheng Analysis of thermal stress and fatigue fracture for the solar tower molten salt receiver Appl. Therm. Eng., 99 (2016), pp. 741-750.

48. R.Z. Wang, X.C. Zhang, J.G. Gong, X.M. Zhu, S.T. Tu, C.C. Zhang Creep-fatigue life prediction and interaction diagram in nickel-based GH4169 superalloy at 650 °C based on cycle-by-cycle concept Int. J. Fa., 97 (2017), pp. 114-123.

49. L. MataveliSuave, J. Cormier, D. Bertheau, P. Villechaise, A. Soula, Z. Hervier, F. Hamon High temperature low cycle fatigue properties of alloy 625 Mater. Sci. Eng., 650 (2016), pp. 161-170.

50. G.J. Kolb An Evaluation of Possible Next-Generation High Temperature Molten-Salt Power Towers SAND2011 9320., Albuquerque, New Mexico (2011).

51. C.R. Brinkman, J.P. Strizak, M.K. Booker Time-dependent strain-controlled fatigue behavior of annealed 2 1/4 Cr-1 Mo steel for use in nuclear steam generator design J. Nucl. Mater., 62 (1976), pp. 181-204.

52. J.J. De Barbadillo, B.A. Baker, R.D. Gollihue, S.A. McCoy Properties of inconel alloy 740H for high pressure steam and supercritical CO2 applications ASME Symp. Elev. Temp. Appl. Mater. Foss. Nucl. Petrochemical Ind. ETAM2018 (2018), pp. 1-11.

53. W.M. Payten, K.U. Snowden, D.W. Dean Effects of prior stress relaxation on the prediction of creep life using time and strain-based methods J. Pressure Vessel Technol., 135 (2013), pp. 1-8.

54. Du, Shen, Zexiao Wang, and Sheng Shen. "Thermal and structural evaluation of composite solar receiver tubes for Gen3 concentrated solar power systems." *Renewable Energy* 189 (2022): 117-128.

55. M. Mehos, C. Turchi, J. Vidal, M. Wagner, Z. Ma, C. Ho, W. Kolb, C. Andraka, A. Kruizeng a Concentrating Solar Power Gen3 Demonstration Roadmap National Renewable Energy Lab (2017).

56. Y.-L. He, Y. Qiu, K. Wang, F. Yuan, W.-Q. Wang, M.-J. Li, J.-Q. Guo Perspective of concentrating solar power Energy, 198 (2020), Article 117373.

57. T. Conroy, M.N. Collins, R. Grimes A review of steady-state thermal and mechanical modelling on tubular solar receivers Renew. Sustain. Energy Rev., 119 (2020), Article 109591.

58. T.W. Neises, M.J. Wagner, A.K. Gray Structural Design Considerations for Tubular Power Tower Receivers Operating at 650 C American Society of Mechanical Engineers (2014).

59. B. Onuike, B. Heer, A. Bandyopadhyay Additive manufacturing of Inconel 718—copper alloy bimetallic structure using laser engineered net shaping (LENS™) Addit. Manuf., 21 (2018), pp. 133-140.

60. R. Powell, R. Tye, M. Hickman the thermal conductivity of nickel Int. J. Heat Mass Tran., 8 (5) (1965), pp. 679-688.

61. M. Grujicic, H. Zhao Optimization of 316 stainless steel/alumina functionally graded material for reduction of damage induced by thermal residual stresses Mater. Sci. Eng., A, 252 (1) (1998), pp. 117-132.

62. Hakeem, Abbas Saeed, et al. "Comparative evaluation of thermal and mechanical properties of nickel alloy 718 prepared using selective laser melting, spark plasma sintering, and casting methods." *Journal of Materials Research and Technology* 12 (2021): 870-881.

63. Onuike, Bonny, and Amit Bandyopadhyay. "Additive manufacturing of Inconel 718–Ti6Al4V bimetallic structures." *Additive Manufacturing* 22 (2018): 844-851.

64. Parida, Asit Kumar, and Kalipada Maity. "Comparison the machinability of Inconel 718, Inconel 625 and Monel 400 in hot turning operation." *Engineering Science and Technology, an International Journal* 21.3 (2018): 364-370.

65. Popovich, Anatoly A., et al. "Microstructure and mechanical properties of Inconel 718 produced by SLM and subsequent heat treatment." *Key Engineering Materials*. Vol. 651. Trans Tech Publications Ltd, 2015.

66. Demetriou, Velissarios, et al. "Study of the effect of hydrogen charging on the tensile properties and microstructure of four variant heat treatments of nickel alloy 718." *international journal of hydrogen energy* 42.37 (2017): 23856-23870.

67. F. Caiazzo, V. Alfieri, G. Corrado, P. Argenio Mechanical properties of Inconel 718 in additive manufacturing via selective laser melting: an investigation on possible anisotropy of

tensile strength 2017 IEEE 3rd international forum on Research and technologies for society and industry (RTSI) (2017), pp. 1-4.

68. H. Wu, D. Zhang, B. Yang, C. Chen, Y. Li, K. Zhou, *et al* Microstructural evolution and defect formation in a powder metallurgy nickel-based superalloy processed by selective laser melting J Mater Sci Technol, 36 (2020), pp. 7-17.

69. K.-S. Kim, S. Yang, M.-S. Kim, K.-A. Lee Effect of post heat-treatment on the microstructure and high-temperature oxidation behavior of precipitation hardened IN738LC superalloy fabricated by selective laser melting J Mater Sci Technol, 76 (2021), pp. 95-103.

70. D. Herzog, V. Seyda, E. Wycisk, C. Emmelmann Additive manufacturing of metals Acta Mater, 117 (2016), pp. 371-392.

71. H. Helmer, A. Bauereiß, R.F. Singer, C. KörnerGrain structure evolution in Inconel 718 during selective electron beam melting Mater Sci Eng, A, 668 (2016), pp. 180-187.

72. Q. Jia, D. Gu Selective laser melting additive manufacturing of Inconel 718 superalloy parts: densification, microstructure and properties J Alloys Compd, 585 (2014), pp. 713-721.

73. C. Pei, D. Shi, H. Yuan, H. Li Assessment of mechanical properties and fatigue performance of a selective laser melted nickel-base superalloy Inconel 718 Mater Sci Eng, A, 759 (2019), pp. 278-287.

74. A. Keshavarzkermani, M. Sadowski, L. Ladani Direct metal laser melting of Inconel 718: process impact on grain formation and orientation J Alloys Compd, 736 (2018), pp. 297-305.

75. G. Marchese, E. Bassini, M. Calandri, E.P. Ambrosio, F. Calignano, M. Lorusso, *et al.* Microstructural investigation of as fabricated and heat-treated Inconel 625 and Inconel 718 fabricated by direct metal laser sintering: contribution of Politecnico di Torino and Istituto Italiano di Tecnologia (IIT) di Torino Met Powder Rep, 71 (2016), pp. 273-278

76. Seedhouse, E. In *SpaceX: making commercial spaceflight a reality* (Springer Science & Business Media, 2013).

77. Joshi, S. C. & Sheikh, A. A. 3D printing in aerospace and its long-term sustainability. *Virtual Phys. Prototyp.* 10, 175–185 (2015).

78. Pollock, T. M. Alloy design for aircraft engines. *Nat. Mater.* 15, 809–815 (2016).

79. Chen, Y. *et al*. Laser powder deposition of carbon nanotube reinforced nickel-based superalloy Inconel 718. *Carbon* 107, 361–370 (2016).

80. Abioye, T., Farayibi, P., McCartney, D. & Clare, A. Effect of carbide dissolution on the corrosion performance of tungsten carbide reinforced Inconel 625 wire laser coating. *J. Mater. Process. Technol.* 231, 89–99 (2016).

81. Liu, Z. *et al*. Ultrathin high-temperature oxidation-resistant coatings of hexagonal boron nitride. *Nat. Comm.* 4 (2013).

82. Pompei, E., Magagnin, L., Lecis, N. & Cavallotti, P. Electrodeposition of nickel–BN composite coatings. *Electrochim. Acta* 54, 2571–2574 (2009).

83. Pompei, E., Magagnin, L., Lecis, N. & Cavallotti, P. Electrodeposition of nickel–BN composite coatings. *Electrochim. Acta* 54, 2571–2574 (2009).

84. Lee, B., Lee, D., Lee, J. H., Ryu, H. J. & Hong, S. H. Enhancement of toughness and wear resistance in boron nitride nanoplatelet (BNNP) reinforced Si_3N_4 nanocomposites. *Sci. Rep.* 6, 27609 (2016).

85. Shrestha, N. K., Sakurada, K., Masuko, M. & Saji, T. Composite coatings of nickel and ceramic particles prepared in two steps. *Surf. Coat. Technol.* 140, 175–181 (2001).

86. Rawal, S. P. Metal-matrix composites for space applications. *JOM* 53, 14–17 (2001).

87. Kim, Sang Hoon, et al. "Thermo-mechanical improvement of Inconel 718 using ex situ boron nitride-reinforced composites processed by laser powder bed fusion." *Scientific reports* 7.1 (2017): 1-13.

88. Zhang, H. L., et al. "Concentrated solar power plants: Review and design methodology." *Renewable and sustainable energy reviews* 22 (2013): 466-481.

89. Rajendran, Duraisamy Ramalingam, et al. "Review on influencing parameters in the performance of concentrated solar power collector based on materials, heat transfer fluids and design." *Journal of Thermal Analysis and Calorimetry* 140.1 (2020): 33-51.

90. Islam, Md Tasbirul, et al. "A comprehensive review of state-of-the-art concentrating solar power (CSP) technologies: Current status and research trends." *Renewable and Sustainable Energy Reviews* 91 (2018): 987-1018.

91. Ho, Clifford K. "Advances in central receivers for concentrating solar applications." *Solar energy* 152 (2017): 38-56.

92. Martinek, Janna, and Zhiwen Ma. "Granular flow and heat-transfer study in a near-blackbody enclosed particle receiver." *Journal of Solar Energy Engineering* 137.5 (2015).

93. López-Herraiz, María, et al. "Effect of the optical properties of the coating of a concentrated solar power central receiver on its thermal efficiency." *Solar Energy Materials and Solar Cells* 159 (2017): 66-72.

BIOGRAPHICAL SKETCH

Naznin Nuria Afrin was born in Dhaka city in Bangladesh. Naznin had enrolled at the University of Texas Rio Grande Valley to pursue her Master of Science in Engineering (MSE) in Manufacturing Engineering in August 2020. At the same time, she also joined the Additive Manufacturing and Bioprinting lab as a graduate research assistant, and she has been assigned to the US Department of Energy SIPS program, collaborating with two other teams from University of Arizona and Mississippi State university, where she was doing research on developing and Fabricating Solar Absorber Tube with internal fin structure using Selective Laser Melting 3D printing and Additive Manufacturing technology.

During the summer of 2022, she worked as a Neutron Imaging Process Intern at Oak Ridge National Laboratory at the High Flux Isotope Reactor (HFIR) and Spallation Neutron Source (SNS), where she was working under supervision of Neutron Instrument scientists on Development of advanced Neutron imaging techniques to characterize and analyze Additively Manufactured products and their morphology, crystal structure, tensile properties with the large instrumental facilities at the national laboratory, and analyzed the collected data with the LINUX software Amira for 3D & 4D data visualization, and processing.

Naznin successfully completed her Master of Science and Engineering in Manufacturing Engineering on December 9th , 2022.

She can be reached at nazninnuriaafrin@gmail.com.